Volume 58
Number 18
4 March 2022
Pages 2933–3074

ChemComm

Chemical Communications

rsc.li/chemcomm

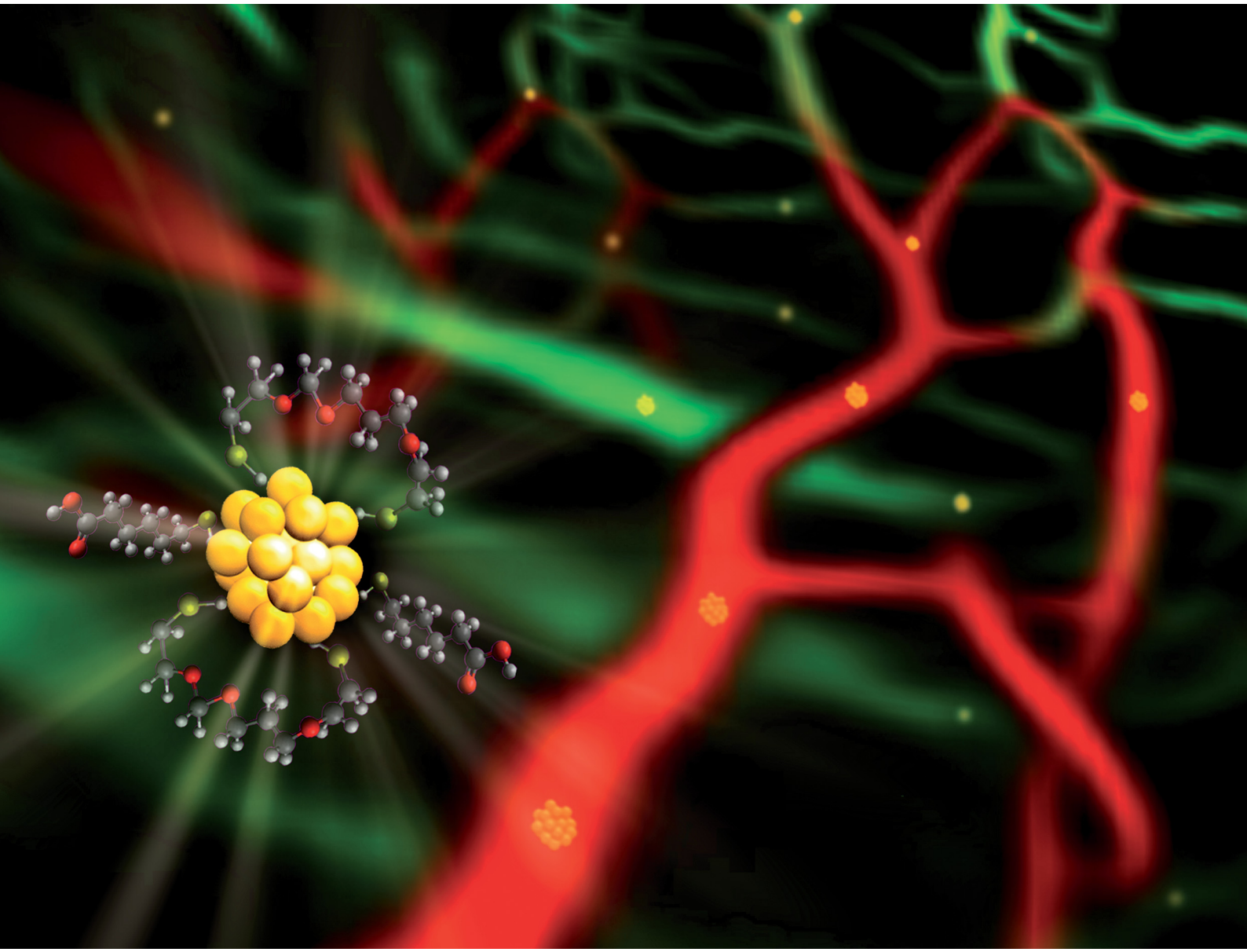

ISSN 1359-7345

ROYAL SOCIETY OF CHEMISTRY

COMMUNICATION

Xavier Le Guével *et al.*

Tailoring the SWIR emission of gold nanoclusters by surface ligand rigidification and their application in 3D bioimaging

ChemComm

COMMUNICATION

View Article Online
View Journal | View Issue

Cite this: *Chem. Commun.*, 2022, **58**, 2967

Received 15th December 2021,
Accepted 4th February 2022

DOI: 10.1039/d1cc07055j

rsc.li/chemcomm

Tailoring the SWIR emission of gold nanoclusters by surface ligand rigidification and their application in 3D bioimaging†

Xavier Le Guével, ‡*[a] K. David Wegner, ‡[b] Christian Würth,[b] Vladimir A. Baulin,[c] B. Musnier,[a] V. Josserand,[a] U. Resch-Genger[b] and Jean-luc Coll[a]

The influence of solvent polarity and surface ligand rigidification on the SWIR emission profile of gold nanoclusters with an anistropic surface was investigated. A strong enhancement of the SWIR emission band at 1200 nm was observed when measuring in different local environments: in solution, in polymer composites, and in solids. SWIR *in vivo* imaging of mice assisted by deep learning after intravenous administration of these gold nanoclusters provides high definition pseudo-3D views of vascular blood vessels.

The shortwave infrared (SWIR), also called NIR-II, between 900 and 1700 nm is an appealing optical window for *in vivo* imaging thanks to reduced tissue scattering and low autofluorescence background.[1] In comparison to the NIR-I window (700–900 nm), photoluminescence (PL) signals can be detected in deeper tissue areas.[2,3] This has led to the development of a variety of SWIR contrast agents based on organic scaffolds such as the indocyanine family,[4] BODIPY,[5] D–A–D structure[6] and AIEgens,[7] and also inorganic probes like lanthanide-based-nanoparticles,[8] quantum dots,[9] or metal (Au, Ag, Cu) nanoclusters (NCs).[10,11] In particular, Au NCs are promising candidates as efficient SWIR emitters because their absorbance/emission profiles in the NIR-I/SWIR can be modulated by controlling their size (*i.e.* number of atoms) and their surface chemistry.[12,13] The strong sensitivity of the PL properties towards the surface architecture was recently shown by adding a short dithiol polyethyleneglycol molecule on the surface of Au_{23} NC. This promoted the emergence of two absorption bands in the NIR-I and an enhanced PL intensity in the SWIR.[12] Other studies have demonstrated how increasing the rigidity of the organic shell surrounding the gold core of Au NC led to a striking enhancement and a blue-shift of the PL signal in the red window (650–850 nm).[14,15] The origin of the multiple SWIR PL bands observed for various Au NCs[12,13,16–18] is still unclear and there is still a lack of information on their sensitivity to the environment such as pH, salt concentration, temperature, and viscosity.

To shed more light into the influence of the microenvironment on the PL properties, we investigated the effect of solvent polarity and rigidification of the surface ligands. Additionally, we illustrate the use of this contrast agent for 3D visualization of vascularization in mice. For these experiments, we used Au NCs stabilized with mercaptohexanoic acid (MHA) and as co-ligand dithiol tetraethyleneglycol (TDT) in an equimolar ratio. Further details about the synthesis procedure can be found in the ESI.† The water-soluble compound AuMHA/TDT possessed strong photostability, a long colloidal stability over weeks. Furthermore, their stability in biological conditions and their low cytotoxicity enabled their use *in vivo* in small animals for biomedical applications as previously reported.[10,12] These NCs show an increasing absorption from the NIR to the UV and interestingly a significant absorption band at 1100 nm, which is not present in absence of the co-ligand TDT and they show nearly no batch-to-batch variation (see Fig. 1A), and (ESI,† Fig. S1). The appearance of this band is hypothesized to be induced by structural micro-distortions on the Au NCs surface.[19] Of note, the maximum of this absorption band is shifted in our case from 980 nm to 1100 nm. This band does not show significant changes over a wide range of pH levels from 4 to 7.5, underlining the stability of the formed Au NC (Fig. S2, ESI†). To exclude that this band appears due to self-assembly of the Au NCs or to bigger plasmonic gold nanoparticles, high-resolution transmission electron microscopy (HRTEM) was performed. Due to interparticle distances larger than 2 nm, covalent cross-linking between Au NCs by the dithiol molecule TDT can be excluded, and thus any photophysical interaction between the NCs. The size of the AuMHA/TDT NCs was estimated to *ca.* 1.4 ± 0.3 nm (see Fig. S3, ESI†).

To investigate the effect of solvent polarity on the optical properties, absorbance and PL measurements were performed

[a] *Institue for Advanced Biosciences, University Grenoble Alpes, CNRS UMR5309, INSSERM U1209, Allée des Alpes 38700, La Tronche, France. E-mail: xavier.le-guevel@univ-grenoble-alpes.fr*
[b] *Federal Institute of Materials Research and Testing (BAM), 12489 Berlin, Germany*
[c] *Departament Química Física i Inorgànica, Universitat Rovira i Virgili, Marcel.lí, Domingo s/n, 43007 Tarragona, Spain*

† Electronic supplementary information (ESI) available. See DOI: 10.1039/d1cc07055j
‡ Authors equally contributed in the work.

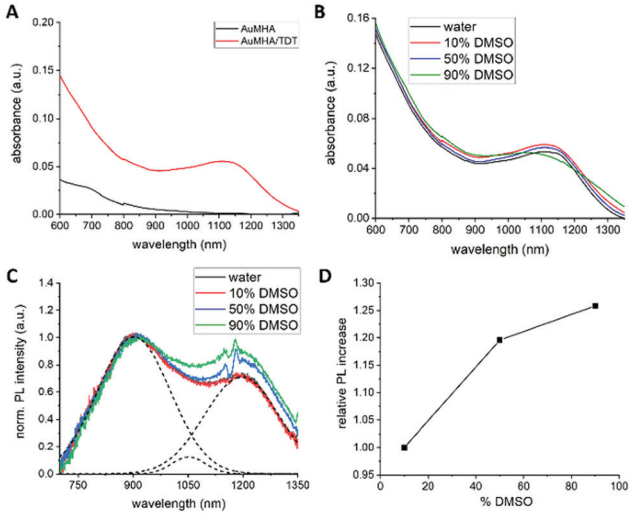

Fig. 1 (A) Absorbance spectra of AuMHA and AuMHA/TDT. (B) Absorbance spectra of AuMHA/TDT NCs with increasing DMSO concentration. (C) Corrected PL emission spectra of AuMHA/TDT NCs with increasing DMSO concentrations and the linear deconvoluted fit of the PL spectra in absence of DMSO (dashed lines). (D) Increase of PL intensity of the PL band at 1250 nm with increasing DMSO concentrations.

with AuMHA/TDT NCs dispersed in different DMSO/water volume ratios from 0 to 90% DMSO. We chose DMSO as co-solvent because of the solubility of these NCs in this solvent, the good miscibility with water, and the decrease of polarity (δ = 0.444) compared to water. The presence of DMSO did not alter the absorbance spectra of the AuMHA/TDT NCs, indicating that the overall cluster structure did not change, and no enhanced ligand desorption occurred (see Fig. 1B).

However, the PL of AuMHA/TDT NCs was clearly affected by increasing the DMSO concentration. The raw PL spectra measured at similar NC concentration, shown in ESI,† Fig. S5 indicated the presence of three major PL bands located at 920 nm, 1050 nm, and 1200 nm using either 680 nm or 830 nm as excitation wavelength.

By normalization on the first band, an increase in the contribution of the 1050 nm and 1200 nm PL band was observed (see ESI,† Fig. S5b and d). But those PL spectra need to be corrected for water and DMSO reabsorption effects, which caused, for example, the dip at 1120 nm. The corrected PL spectra with increasing DMSO concentration normalized on the PL band at 920 nm are shown in Fig. 1C. The spectra were further linear deconvoluted to estimate the contribution of each band in the overall PL spectrum. An example of such deconvolution is also shown in Fig. 1C as dashed lines for AuMHA/TDT NCs in pure water. Plotting the PL intensity of the PL band at 1200 nm over the increasing DMSO concentration resulted in a linear dependency, which indicates that this band can be associated to energy transfers involving the surface ligands and the Au NCs (see Fig. 1D). A possible explanation for this effect can be the dependency of the charge transfer efficiency on the differences between the dielectric constant of the medium and the ligand shell. By increasing the amount of DMSO in solution, a solvent with a lower dielectric constant, the Fermi level of the Au NCs increases. This increases the charge density at the interface, which increases the interfacial bonding interaction between Au NC core and its ligands. To exclude an impact of viscosity of the solvent and confirm the contribution of dielectric constant, we also measured the PL of AuMHA/TDT in a mixture DMF/water. Indeed, DMSO has a viscosity slightly higher (2cP) than water (1cP) or DMF (0.79cP) while the dielectric constant of DMF is 36.71 F m^{-1}, which is half of the dielectric constant of water with 78.4 F m^{-1} but closer to DMSO with 46.68 F m^{-1}. The absorbance spectra shown in Fig. S6a (ESI†) of the Au NCs reveal that upon mixing with DMF, the NC structure does not change and the enhanced absorbance feature at 1100 nm can still be observed. Similar to the measurements in presence of DMSO, the Au NCs in 50% and 90% DMF were excited at 680 nm and at 830 nm and the PL spectra were measured (Fig. S6, ESI†). Although the increase of the PL bands at 1050 nm and 1200 nm with increasing DMF concentration is not as strong as for the measurement with DMSO, we can observe a significant increase of these PL bands. This shows that this effect is induced by differences in solvent polarity than by viscosity differences of the solvent. Therefore, these changes in the electronic properties can be a potential explanation for the changes in the charge transfer efficiencies affecting the PL band composition.[20]

Knowing that the choice of the excitation wavelength can favour specific energy transitions within the AuNCs,[21] the samples were measured with different excitation wavelengths (Fig. S7, ESI†). Interestingly the observed trend still remained, which shows that probably multiple energy transfer can take place in the SWIR window.[12]

To further manipulate the microenvironment of the surface ligands, PL measurements were performed in presence of proteins such as bovine serum albumin (BSA) or in more complex media such as serum. It can be expected that a corona is formed around the Au NCs, which can affect the PL properties in two ways: either the protein–ligand adsorption result in a steric hindrance of the ligands rotation or the difference in the static permittivity of the BSA solution result in a similar effect as observed for the addition of DMSO.[22] In contrast to the measurement in DMSO, the contribution of the PL band at 1200 nm was not enhanced (see ESI,† Fig. S8). In addition, previous PAGE electrophoresis measurements of AuMHA/TDT in pure water or in presence of BSA did not differ, suggesting the absence of a strong interaction between BSA and the Au NCs.[10] This indicates that interactions between BSA and AuMHA/TDT are rather weak which could be explained by the presence of the polyethyleneglycol chain in TDT co-ligand acting as anti-fouling agent[10,23] or by the smaller size of AuMHA/TDT compare to BSA (66.3 kDa; ~7 nm).

In order to determine if the rigidification of the surface ligands influences the PL properties of AuMHA/TDT NCs, lyophilised Au NCs were mixed with polymethoxysilane (PDMS) to create a composite as seen in Fig. 2A. In comparison to the Au NCs in solution, the Au NCs in the composite possessed much stronger absolute PL intensities as shown in Fig. S9

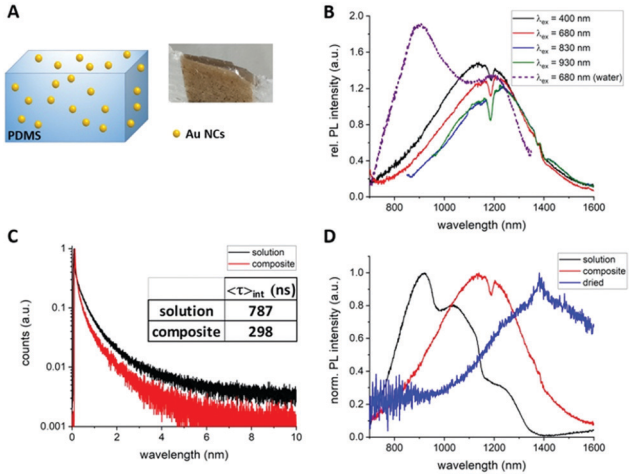

Fig. 2 (A) Composite made of AuMHA/TDT NCs in PDMS. (B) SWIR PL emission spectra of the composite at different excitation wavelength and in water at 680 nm excitation for comparison. (C) Fluorescence lifetime measurement of composite and AuMHA/TDT in water. ($\lambda_{exc.}/\lambda_{em.}$= 375 nm/920 nm). (D) SWIR PL emission spectra of AuHA/TDT NCs in solution, in composite, in dried solid state ($\lambda_{exc.}$= 375nm).

(ESI†). The PL spectrum of Au NCs in the composite was substantially different from the one in solution with the PL emission at 920 nm vanishing and with a maximum emission centred at ~1200 nm (Fig. 2B). This PL emission maximum was dependent on the excitation wavelength with a bathochromic shift from 1150 nm ($\lambda_{exc.}$ = 400 nm) to 1250 nm ($\lambda_{exc.}$ = 930 nm) (see Fig. 2B). Time-resolved measurements of the Au NCs in the composite and in solution showed a reduced fluorescence lifetime with $\langle\tau\rangle_{int.}$= 298 ns and 787 ns, respectively (Fig. 2C and Table S1, ESI†). It can be assumed that the reduced lifetime can be associated with an increase in non-radiative recombination by the rigid environment, which was also observed for other luminescent probes when they are embedded in composites.[24] We also attempted to measure the photophysical properties of the Au NCs at very harsh condition of rigidification by mild casting the solution on a glass slide and dry off any solvents before. Fig. 2D shows the comparison of the PL spectra of Au MHA/TDT NCs in solution, in the composite, and in quasi solid state. A striking bathochromic shift of the PL maximum from 920 nm (solution) to 1200 nm (composite) and then 1450 nm (solid) was observed. Additionally, the PL profile in composite and solid state have nearly a Gaussian shape while multiple PL bands are visible in solution.

The origin of the SWIR PL band transitions are still under debate but energy transfers are taking place: (1) from both the metal core[13,18] *via* the aurophilic interaction, and (2) from the surface *via* metal-to-thiolated ligands interaction.[16,25,26] By modifying the polarisation and the rigidity of the microenvironment of Au NCs with anisotropic surfaces, we reveal the high sensitivity of the PL band centred at 1200 nm to these parameters. The microsecond range of the fluorescence lifetime and the wavelength dependency of this SWIR PL also suggest that multiple energy transitions are involved during the emission process. In a different study, Huang *et al.* attributed a strong red PL intensity of Au NCs loaded in a silica matrix to electronic-coupling-enhanced radiative rates and covalent-bonding-suppressed nonradiative relaxation.[27] The even longer 200 nm bathochromic shift of PL to 1450 nm which is reported here might be also associated to the surface modification but also a change of Au NC structure could happen during the casting process. With the red-shift and the enhancement of SWIR PL of this probe to the NIR-IIa region (1200–1400 nm) region in more complex environments, we are expecting high levels of detection at high concentrations in blood.

To demonstrate the potential of this contrast agent, which exhibit SWIR PL above 1300 nm, we perfused a mouse with AuMHA/TDT (see ESI,† for the experimental detail) and performed SWIR imaging on a tilted support by varying the angles from −45° to +45° with 0.5° step (Fig. 3A). SWIR images were collected in the range 1319–1700 nm using an 808 nm excitation laser (120 mW cm^{-2}) and a 25 mm lens at 4.8 numerical aperture. The segmentation of the vessels from the background was performed using IterNet neural network (IterNet: Retinal Image Segmentation Utilizing Structural Redundancy in Vessel Networks), which was applied to SWIR images as described in ref. 2. The output of this segmentation is the probability of finding a vessel. We can see a 3D reconstruction obtained of the ventral side of a whole mouse with a clear view of the main blood vessels in Fig. 3B and movie 1 (ESI†). The image processing enabled to choose a signal threshold and visualize only the vessels without fluorescence from the tissue. Hence, the vascular network could be nicely seen at different angles at different depths (Fig. 3C, movie 2, ESI†). In further image

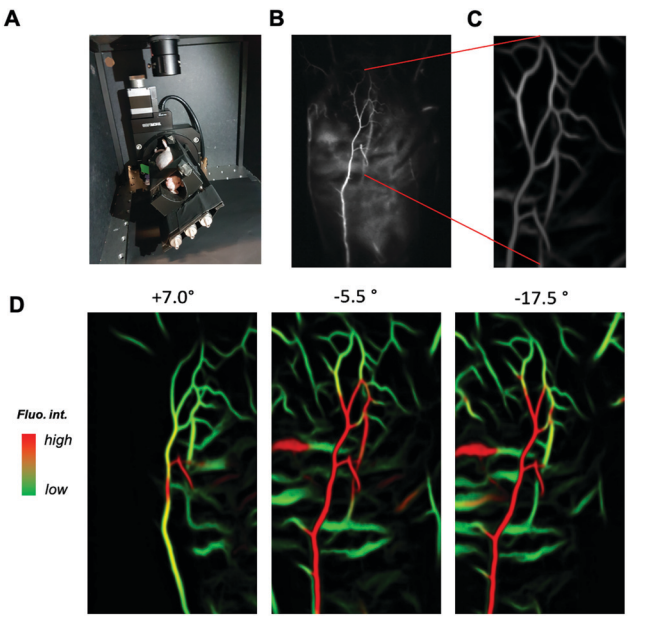

Fig. 3 (A) SWIR *in vivo* imaging set up for 3D imaging. (B) SWIR imaging of perfused mouse at full scale, and (C) processed by deep learning. (D) Different angles showing different signal level in tissue and in blood vessels. Segmented blood vessels network at higher magnification shows pseudo-3D localization of blood vessels.

treatment large vessels (higher probability corresponds to higher fluorescence intensity) are shown in red, while the green colour is assigned to vessels with lower intensities (small vessels network structure) (see Fig. 3D). Since the output of the segmentation is the probability, it is possible to increase the magnification on the post-treated images and visualize the blood vessels at the micrometric scale with a 3D view created from tilting the camera around the mice (movie 2, ESI†).

In conclusion, we showed here how the SWIR PL band contributions in the PL spectrum of AuMHA/TDT NCs can be modulated depending on the solvent polarization and rigidification of the surrounding. A key advancement is the observed sensitivity of the PL band at 1200 nm towards the microenvironment. This long SWIR shift of Au NCs opens new perspectives for more sensitive probes necessary for NIR-IIb (1500–1700 nm) *in vivo* imaging. We illustrate for the first time the ability to perform 3D fluorescence imaging reconstruction assisted by deep learning using a simple equipment that permits a sharp overview of the vascular network in a whole mouse.

X. L. G. would like to thank Ines Häusler for the TEM measurement, Maxime Henry and Julien Vollaire for the animal experimentation. X. L. G. would like to thank Plan Cancer (C18038CS) and ligue contre le cancer (R21004CC) for their financial support. X. L. G. and U. R. thank ANR SIREN (ANR-20-CE92—0039-01) for their financial support. VAB acknowledges financial assistance from the Ministerio de Ciencia, Innovación y Universidades of the Spanish Government through research project PID2020-114347RB-C33, financed by MCIN/AEI 10.13039/501100011033.

Conflicts of interest

Authors declare they have no conflicts of Interest.

Notes and references

1 G. Hong, A. Antaris and H. Dai, *Nat. Biomed. Eng.*, 2017, **1**, 0010 (0011-0022).
2 V. A. Baulin, Y. Usson and X. Le Guével, *J. Biophotonics*, 2021, e202100102.
3 B. Musnier, M. Henry, J. Vollaire, J.-L. Coll, Y. Usson, V. Josserand and X. Le Guével, *J. Biophotonics*, 2020, e202000345.
4 S. Wang, Y. Fan, D. Li, C. Sun, Z. Lei, L. Lu, T. Wang and F. Zhang, *Nat. Commun.*, 2019, **10**, 1058.
5 A. Godard, G. Kalot, J. Pliquett, B. Busser, X. Le Guével, K. D. Wegner, U. Resch-Genger, Y. Rousselin, J.-L. Coll, F. Denat, E. Bodio, C. Goze and L. Sancey, *Bioconjugate Chem.*, 2020, **31**, 1088–1092.
6 Q. Yang, H. Ma, Y. Liang and H. Dai, *Acc. Mater. Res.*, 2021, **2**, 170–183.
7 W. Xu, D. Wang and B. Z. Tang, *Angew. Chem., Int. Ed.*, 2021, **60**, 7476–7487.
8 Y. Yang, D. Tu, Y. Zhang, P. Zhang and X. Chen, *iScience*, 2021, **24**, 102062.
9 H. Yang, R. Li, Y. Zhang, M. Yu, Z. Wang, X. Liu, W. You, D. Tu, Z. Sun, R. Zhang, X. Chen and Q. Wang, *J. Am. Chem. Soc.*, 2021, **143**, 2601–2607.
10 Z. Yu, B. Musnier, K. D. Wegner, M. Henry, B. Chovelon, A. Desroches-Castan, A. Fertin, U. Resch-Genger, S. Bailly, J.-L. Coll, Y. Usson, V. Josserand and X. Le Guével, *ACS Nano*, 2020, **14**, 4973–4981.
11 Y. Kong, D. Santos-Carballal, D. Martin, N. N. Sergeeva, W. Wang, G. Liu, B. Johnson, B. Bhayana, Z. Lin, Y. Wang, X. Le Guével, N. H. de Leeuw, D. Zhou and M. X. Wu, *Mater. Today*, 2021, **51**, 96–107.
12 B. Musnier, K. D. Wegner, C. Comby-Zerbino, V. Trouillet, M. Jourdan, I. Hausler, R. Antoine, J. L. Coll, U. Resch-Genger and X. Le Guevel, *Nanoscale*, 2019, **11**, 12092–12096.
13 Q. Li, D. Zhou, J. Chai, W. Y. So, T. Cai, M. Li, L. A. Peteanu, O. Chen, M. Cotlet, X. Wendy Gu, H. Zhu and R. Jin, *Nat. Commun.*, 2020, **11**, 2897.
14 K. Pyo, V. D. Thanthirige, K. Kwak, P. Pandurangan, G. Ramakrishna and D. Lee, *J. Am. Chem. Soc.*, 2015, **137**, 8244–8250.
15 X. Le Guével, O. Tagit, C. E. Rodríguez, V. Trouillet, M. Pernia Leal and N. Hildebrandt, *Nanoscale*, 2014, **6**, 8091–8099.
16 Y. Chen, D. Montana, H. Wei, J. Cordero, M. Schneider, X. Le Guevel, O. Chen, O. Bruns and M. Bawendi, *Nano Lett.*, 2017, **17**, 6330–6334.
17 Q. Li, C. J. Zeman Iv, Z. Ma, G. C. Schatz and X. W. Gu, *Small*, 2021, **17**, 2007992.
18 M. Zhou and Y. Song, *J. Phys. Chem. Lett.*, 2021, **12**, 1514–1519.
19 X. Yuan, N. Goswami, W. Chen, Q. Yao and J. Xie, *Chem. Commun.*, 2016, **52**, 5234–5237.
20 A. Cirri, A. Silakov, L. Jensen and B. J. Lear, *J. Am. Chem. Soc.*, 2016, **138**, 15987–15993.
21 Z. Liu, Z. Wu, Q. Yao, Y. Cao, O. J. H. Chai and J. Xie, *Nano Today*, 2021, **36**, 101053.
22 J. Eden, P. R. C. Gascoyne and R. Pethig, *J. Chem. Soc., Faraday Trans. 1*, 1980, **76**, 426–434.
23 T. D. Fernandez, J. R. Pearson, M. Pernia Leal, M. J. Torres, M. Blanca, C. Mayorga and X. Le Guével, *Biomater.*, 2015, **43**, 1–12.
24 A. Reisch, P. Didier, L. Richert, S. Oncul, Y. Arntz, Y. Mély and A. S. Klymchenko, *Nat. Commun.*, 2014, **5**, 4089.
25 S. E. Crawford, C. M. Andolina, A. M. Smith, L. E. Marbella, K. A. Johnston, P. J. Straney, M. J. Hartmann and J. E. Millstone, *J. Am. Chem. Soc.*, 2015, **137**, 14423–14429.
26 S. E. Crawford, M. J. Hartmann and J. E. Millstone, *Acc. Chem. Res.*, 2019, **52**, 695–703.
27 H.-Y. Huang, K.-B. Ca, C.-C. Io, P.-W. Chen, R. J. Soebroto, J.-L. Shen, J.-M. Yeh and C.-T. Yuan, *J. Phys. Chem. Lett.*, 2020, **11**, 9344–9350.

